


Rapid U-Pb Geochronology by Laser Ablation Multi-Collector ICP-MS

Kurt E. Sundell* , George E. Gehrels and Mark E. Pecha

Department of Geosciences, University of Arizona, Tucson, AZ, 85721, USA

* Corresponding author. e-mail: sundell@arizona.edu

Detrital zircon (DZ) U-Pb laser ablation-inductively coupled plasma-mass spectrometry (LA-ICP-MS) has revolutionised the way geologists approach many Earth science questions. Although recent research has focused on rapid sample throughput, acquisition rates are limited to 100–300 analyses h⁻¹. We present a method to acquire zircon U-Pb dates at rates of 120, 300, 600 and 1200 analyses h⁻¹ (30, 12, 6 and 3 s per analysis) by multi-collector LA-ICP-MS. We demonstrate the efficacy of this method by analysing twelve zircon reference materials with dates from ~ 3465 to ~ 28 Ma. Mean offset from high-precision dates increases with faster rates from 0.9% to 1.1%; mean random 1 σ uncertainty increases from 0.6% to 1.3%. We tested this new method on a sandstone sample previously characterised by large- n DZ geochronology. Quantitative comparison shows increased correspondence among age distributions comprising > 300 dates. This new method holds promise for DZ geochronology because (a) it requires no major changes to hardware, but rather modifications to software; (b) it yields robust age distributions well-suited for quantitative analysis and maximum depositional age calculations; (c) there is only a minor sacrifice of accuracy and measurement uncertainty; and (d) there is less burden to researchers in terms of time investment and analytical cost.

Keywords: geochronology, detrital zircon, laser ablation, Arizona LaserChron Center, U-Pb.

Received 23 Dec 19 – Accepted 12 Jul 20

Detrital zircon (DZ) U-Pb geochronology by laser ablation-inductively coupled plasma-mass spectrometry (LA-ICP-MS) has revolutionised the way in which many geological studies are conducted (Fedo *et al.* 2003, Gehrels 2014). DZ research has been used to investigate a variety of Earth processes related to questions of tectonic setting (Cawood *et al.* 2012), source-to-sink sediment provenance (Sircombe 1999, Andersen 2005), sediment routing (Whitchurch *et al.* 2011, Blum and Pecha 2014), sediment reworking and recycling (Dickinson *et al.* 2009), depositional age (Dickinson and Gehrels 2009), palaeogeographical reconstructions (Meinhold *et al.* 2013, Soreghan and Gehrels 2000), evolution of early Earth (Compston and Pidgeon 1986), terrane tectonics (Murphy *et al.* 2004), zircon fertility (Moecher and Samson 2006), palaeo-wind directions and loess transport (Soreghan *et al.* 2002, Licht *et al.* 2016), and drivers of palaeoclimate (McKenzie *et al.* 2016). Since early application of mass spectrometry to Earth science, there has been a steady increase in interest and application of generating dates (i.e.,

numbers calculated from isotopic ratios and decay equations) and ages (i.e., calculated dates that have geological significance, such as an interpretive DZ age distribution or maximum depositional age; Schoene 2014). DZ geochronology by LA-ICP-MS affords rapid throughput, high spatial resolution and low-cost acquisition of zircon geochronological and geochemical information. Zircon is ideally suited for interrogating many Earth science questions by its physical robustness and geochemical make-up. Specifically, zircon has a simple chemical formula (ZrSiO₄) that incorporates appreciable amounts of U and little initial Pb (Stacey and Kramers 1975), as well as other measurable trace elements into its mineral structure that are useful for understanding source rock type and crystallisation environment (Belousova *et al.* 2002, 2010). Zircon is ideal for questions involving multiple orogenic cycles (Gehrels 2014), as it is refractory, highly resistant to physical and chemical weathering, stable under a wide range of pressure and temperature conditions, and undergoes little to no post-crystallisation isotopic exchange or high-

temperature re-equilibrium diffusion (Speer 1980, Cherniak *et al.* 1997).

Among many aspects of DZ geochronology, sample size (i.e., the number of individual dates in a single detrital sample, n) is of significant importance (Vermeesch 2004, Pullen *et al.* 2014). Over the years, there has been a punctuated increase in the number of dates used to characterise DZ age distributions. Early research suggested that sixty analyses are satisfactory to adequately characterise the age distribution of a detrital sample (Dodson *et al.* 1988). This modest number largely stemmed from instrumentation limitations, which at the time were restricted to the relatively slower, but higher precision acquisition methods of isotope dilution thermal ionisation mass spectrometry (ID-TIMS) and sensitive high mass-resolution ion microprobe. Following the advent and application of LA-ICP-MS to U-Pb geochronology, researchers began applying statistical methods attempting to quantify how many dates are required to adequately characterise age distributions (Morton *et al.* 1996, Cawood and Nemchin 2001, Vermeesch 2004, Gehrels *et al.* 2006, 2008). Vermeesch (2004) suggested that 117 dates are sufficient to be 95% certain that all age populations representing more than 5% of the total age spectrum had been sampled. However, both empirical investigation and synthetic testing have shown that there is no ideal sample size, but rather the appropriate n is sample-dependent and dictated by sample complexity; multiple groups independently found that $n \approx 100$ is inadequate to characterise most DZ age distributions and that $n \approx 300$ provides a more robust estimate of complex, multimodal age distributions (e.g., Pullen *et al.* 2014, Saylor and Sundell 2016). Still, in studies where maximum depositional age and analysis of the youngest zircon age fraction are critical, larger sample size and/or purposefully biased sample selection may be required (e.g., Pettit *et al.* 2019).

The desire to increase sample size has driven research focused on LA-ICP-MS efficiency and sample throughput, leading to improvements in instrumentation, methodology, data reduction and laboratory protocols (Gehrels *et al.* 2006, 2008, Cottle *et al.* 2009, Johnston *et al.* 2009, Cottle *et al.* 2012, Gehrels 2014, Pullen *et al.* 2014, 2018, Horstwood *et al.* 2016). Advancements have been made in a variety of ways. One major advancement was using total isotopic counts to calculate isotopic ratios, which affords much shorter ablation times, with reasonable uncertainties calculated based on Poisson counting statistics (Cottle *et al.* 2009, 2012), or empirical calibration (Johnston *et al.* 2009). Matthews and Guest (2017)

optimised rapid acquisition detrital geochronology for quadrupole LA-ICP-MS by decreasing background and ablation durations and forgoing cathodoluminescence imaging in lieu of detailed filtering made possible by time-resolved analysis. Cottle *et al.* (2012) developed a technique capable of extracting reliable U-Pb dates from a single laser pulse, affording high-resolution depth profiling (Viete *et al.* 2015). These and other advancements have resulted in routine acquisition of U-Pb dates at rates faster than 100 analyses h^{-1} in many laboratories. More recently, Chew *et al.* (2019) developed a technique that affords ~ 300 analyses h^{-1} by implementing ultrafast ablation frequency (up to 50 Hz). Despite these recent advancements, acquisition rates are still limited to 100–300 analyses h^{-1} .

We present a new method of acquiring U-Pb dates from zircon by multi-collector LA-ICP-MS at rates of 120 analyses h^{-1} (30 s per analysis), 300 analyses h^{-1} (12 s per analysis), 600 analyses h^{-1} (6 s per analysis) and 1200 analyses h^{-1} (3 s per analysis). We provide an overview of data reduction methods for handling and reducing time-resolved U-Th-Pb data from multi-collector LA-ICP-MS. We demonstrate the efficacy of this technique by testing twelve zircon reference materials with dates ranging from ~ 3465 to ~ 28 Ma. We analysed a complex detrital sample using each acquisition rate to demonstrate the benefits of gathering large- n detrital data and to highlight best practices and the appropriateness of different acquisition rates for different geological applications. The new method is accomplished largely through modifications in software (e.g., data acquisition, automation, and reduction methods) and requires only minor adjustments to standard multi-collector LA-ICP-MS hardware, resulting in no additional burden to the user in terms of time investment or analytical cost. Because the focus is on modifications to software, we also contribute a new, open-source data reduction package, *AgeCalcML*, that is capable of handling time-resolved analysis at fast acquisition rates, and available for any researcher or laboratory to use and/or modify as they wish (github.com/kurtsundell/AgeCalcML).

Data acquisition

The methods discussed below are optimised for DZ geochronology and build on established protocols currently employed at the Arizona LaserChron Center (laserchron.org) outlined in Gehrels *et al.* (2006) and Horstwood *et al.* (2016). Sample preparation and methods of mineral separation by rock crushing, pulverising, density and magnetic separation, epoxy mounting and sample imaging follow established procedures outlined in Gehrels *et al.* (2006, 2008).

U-Th-Pb data were gathered using a Photon Machines Analyte-G2 ArF 193 nm excimer laser with a HelEx sample cell connected to a Nu plasma high-resolution (HR) multi-collector mass spectrometer via an aerosol rapid introduction system (ARIS). Ablated material was transported to the mass spectrometer plasma source via He carrier gas and measured using a combined Faraday and ion counter routine that measured ^{238}U , ^{232}Th , ^{208}Pb , ^{207}Pb and ^{206}Pb with Faradays and $^{204}(\text{Pb} + \text{Hg})$ and ^{202}Hg with ion counters (see collector configuration in Table 1). A 30 μm laser spot size was used for the methods and results presented here. All other laser ablation and multi-collector mass spectrometer parameters were not specifically tested in this contribution and are similar to those presented in Pullen *et al.* (2014, 2018; Table 1).

Automated laser schedules for individual measurement sessions were generated using the laser software (*Chromium*). Prior to each session, all selected laser spots on the sample were pre-treated with a three-pulse ‘cleaning shot’ using a 50 μm beam diameter; this method has been shown to be useful in removing common Pb and any other contaminants from the surface of the sample epoxy mount (Pullen *et al.* 2014, 2018), and is critical for rapid acquisition methods discussed in detail below.

Four rates of acquisition were developed and tested for rapid LA-ICP-MS U-Pb geochronology: 120 analyses h^{-1}

(30 s per analysis), 300 analyses h^{-1} (12 s per analysis), 600 analyses h^{-1} (6 s per analysis) and 1200 analyses h^{-1} (3 s per analysis), which equates to 15, 7, 3 and 1 s of sample integration time (Figure 1). Each of these methods was optimised to maximise the on-peak analysis time while minimising the background measurement and analysis washout time (Figure 1). Rapid (< 1 s) sample washout was made possible by application of the ARIS system and removal of the aerosol homogenisation device (mixing bowl) before reaching the mass spectrometer plasma (i.e., the ARIS was connected directly to the front of the torch).

Rapid acquisition requires special attention to indexing of individual Faraday and ion counter measurements (Table 1). All measurement sessions were conducted in time-resolved analysis mode with 0.2-s resolution, where each 0.2-s measurement represented one index (upper x-axes in Figure 1). This value is a compromise between finer (e.g., 0.1 s) and coarser (e.g., 0.5 s) resolutions. Although finer resolution would have less uncertainty in identifying the start of ablation for each sample (time zero, t_0), it results in fewer total ions counted for each individual measurement because each measurement on the Faradays has a 0.03-s settle time before reading any signal, during which no measurement is being made, resulting in 30% signal loss for 0.1-s resolution; only 15% of the signal is lost at 0.2-s resolution. Coarser resolution (e.g., 0.5–1.0 s) yields less signal loss and higher total ions counted, but compromises the reliable determination of t_0 , resulting in significantly higher uncertainty for faster rates of acquisition (grey vertical bars in Figure 1).

Table 1.
Parameters for laser and mass spectrometer

Parameter	Value
Laser	
Type and wavelength	Photon Analyte-G2 193 nm Excimer Laser
Sample cell	HelEx
Constant energy set	7 mJ
Laser energy	100% (open gate)
Repetition rate	7 Hz
MFC1, MFC2 He	0.10, 0.30 l min^{-1}
Pre-ablation pass	Three bursts at 50 μm
Laser beam diameter	30 μm
Mass spectrometer	
Type	Nu Instruments HR Multi-collector
Cool gas	13.0 l min^{-1}
Auxiliary gas	0.80 l min^{-1}
Sample/make-up gas	1.06 l min^{-1}
RF power	1300 W
Masses measured (Faraday)	^{206}Pb , ^{207}Pb , ^{208}Pb , ^{232}Th , ^{238}U
Masses measured (ion counter)	$^{202}(\text{Hg} + \text{Pb})$ and ^{204}Pb
Collector configuration – mass (Faraday)	ExH-238, H2-232, L6-208, L7-207, L8-206
Collector configuration – mass (ion counter)	IC0-204, IC2-202

MFC = mass flow controller.

Data reduction

We developed a new open-source data reduction program in MATLAB, *AgeCalcML* (github.com/kurtsundell/AgeCalcML). The new reduction software and code is largely based on the in-house *Excel Macro AgeCalc* at the Arizona LaserChron Center (Gehrels *et al.* 2008) and follows data reporting protocols recommended by Horstwood *et al.* (2016).

Each isotopic mass was recorded as a discrete time series (Figure 2). Individual analyses were parsed from the seven isotopic time-series measurements by identifying the timing of start of laser ablation, t_0 . The time t_0 for each zircon measurement was determined by the first five consecutive ^{238}U indexes (1 s total) that were greater than a set threshold of -0.004 V (uncorrected Nu plasma high-resolution HR multi-collector Faraday backgrounds are commonly -0.006 to -0.007 V). Identification of t_0 could only be at the resolution of ± 0.2 s (grey shaded areas in Figure 1), so

adjacent indexes were not considered in any subsequent background or ablation (on-peak) calculations.

Establishing t_0 provides a point of reference from which to extract background and on-peak measurements for each individual analysis (Figure 1). Once t_0 was established, slight differences in the parameterisation of

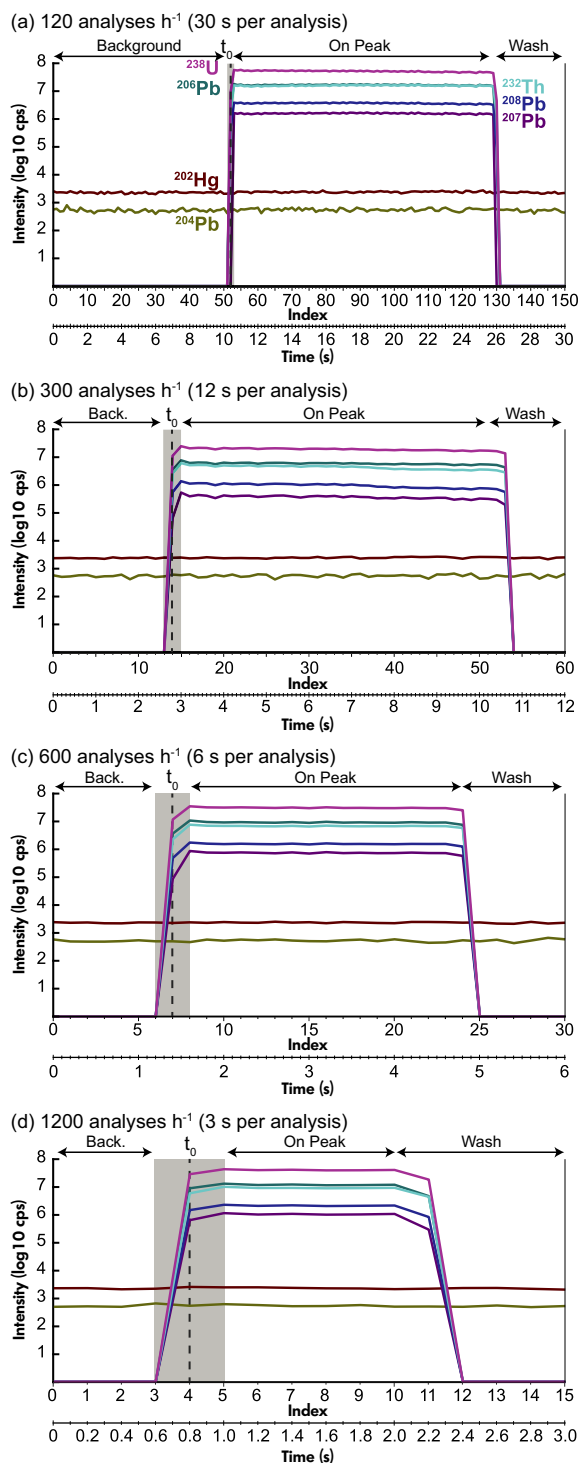


Figure 1. Four methods for rapid acquisition of zircon U-Pb dates at rates of (a) 120 analyses h⁻¹, (b) 300 analyses h⁻¹, (c) 600 analyses h⁻¹ and (d) 1200 analyses h⁻¹. All methods were time-resolved analysis (TRA) at 0.2-s resolution where 1 index = 0.2 s. Data shown here are background subtracted. Time zero (t_0) is the time laser firing begins and has a resolution of ± 0.2 s; background subtraction and on-peak measurements do not include indexes immediately before and after t_0 . Down-hole correction was applied for the 120 analyses h⁻¹ rate due to the long 15-s ablation time; all other acquisition methods used total counts (see Data reduction section). Each plot shows real data from a test measurement session. Wash. = washout. Back. = background.

each of the four acquisition rates allowed for the extraction of isotopic information from the time-series measurements (Table 1). For example, t_0 for the 300 analyses h⁻¹ (12 s per analysis) rate was set to index 14 ± 1 (2.8 ± 0.2 s; Figure 1b). Continuing with the 300 analyses h⁻¹ example, individual analyses were extracted from the raw time series with start and end indexes defined as t_0 index plus forty-six indexes and t_0 index minus thirteen indexes, respectively, totalling sixty indexes (12.0 s; Figure 1b). In this example, background measurements were extracted from the first twelve indexes, and on-peak measurements were extracted from indexes 16 to 50 in order to calculate U-Th-Pb ratios of interest (see Appendix S2, 'Indexing').

Background measurements are calculated differently for each method. Although variable between sessions due to differences in tuning, the background signal is remarkably stable on a multi-collector mass spectrometer (see example in Figure 3). Sufficient background measurement must be made in order to determine measurement uncertainty, which is limited by calculation of standard error of the mean (SE), and as a function of Poisson counting statistics. Counting statistics present a major challenge for developing rapid acquisition techniques. Previous methods have implemented total counts and empirically calibrated Poisson uncertainty (Johnston *et al.* 2009). For the 120 analyses h⁻¹ method, the closest acquisition rate to traditional methods, a total of fifty indexes (10 s) of background are measured and baseline subtracted (BLS) from on-peak measurements (Figure 1a). This brings the SE for ²³⁸U to < 1% (magenta curve in Figure 3). For higher acquisition rates of 300–1200 analyses h⁻¹, the method of measuring backgrounds prior to each analysis with background subtraction on a sample-by-

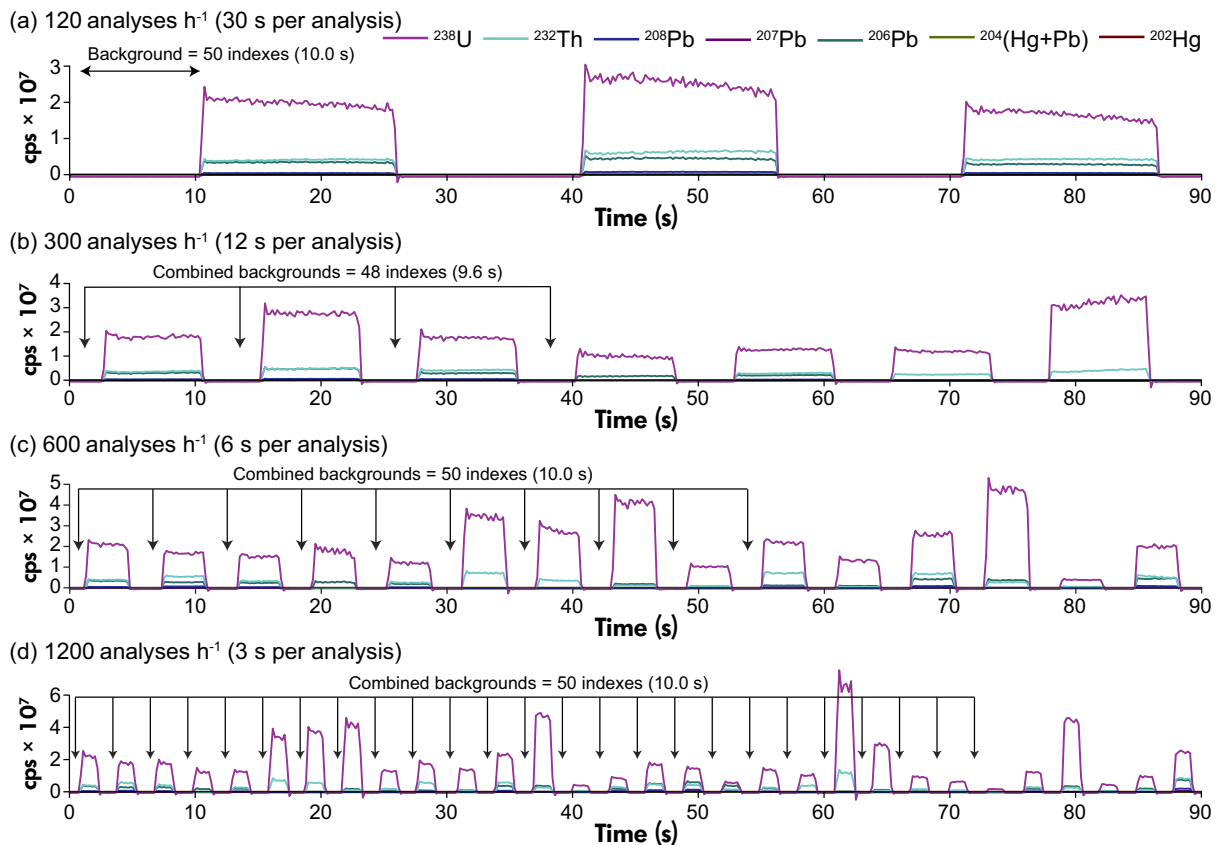


Figure 2. Time-resolved analysis (TRA) plotted as time series for the first 90 s of sample measurement from Session 1 on 19 April 2019. (a) 120 analyses h^{-1} (30 s per analysis): background measurements were applied sample by sample. (b) 300 analyses h^{-1} (12 s per analysis): background measurements are grouped for every four samples. (c) 600 analyses h^{-1} (6 s per analysis): background measurements are grouped for every ten samples. (d) 1200 analyses h^{-1} (3 s per analysis): background measurements are grouped for every twenty-five samples.

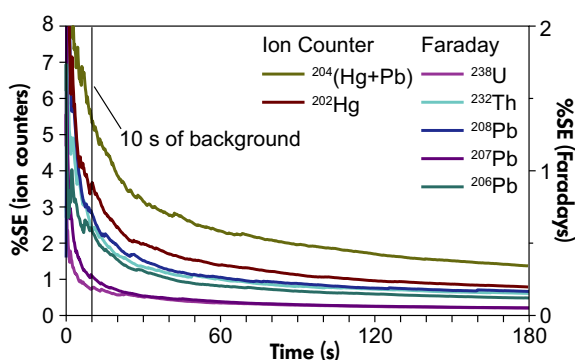


Figure 3. Multi-collector mass spectrometer background measurements for 180 s (900 indexes). The four acquisition methods described herein include 9.6 to 10.0 s (forty-eight to fifty indexes) of background for calculation of mean and standard error (SE).

sample basis is insufficient to bring the SE down to a reasonable level (i.e., < 2%). This is most notable for 1200 analyses h^{-1} where only two indexes (0.4 s) of background are measured for each individual analysis resulting in $SE \gg 1\%$ (Figure 3).

In order to produce reasonable counting statistics for propagation of uncertainties from background subtraction, we implemented a modified approach to background subtraction for methods of 300–1200 analyses h^{-1} wherein background measurements are combined for multiple analyses. For 300 analyses h^{-1} , background measurements are combined for four consecutive analyses yielding a total of forty-eight indexes (9.6 s), from which the mean is calculated and subtracted from on-peak measurements and SE is propagated for the four corresponding analyses. For 600 analyses h^{-1} , 1 s of background measurement (five

indexes) for each analysis is combined over ten consecutive samples, yielding fifty indexes (10.0 s) applied to corresponding ten analyses. For 1200 analyses h⁻¹, 0.4 s of background measurements from twenty-five analyses (fifty total indexes) is combined and applied to corresponding analyses.

We implemented a second (optional) routine to calculate background wherein a sliding window of user-specified width is used to calculate the mean and standard error of background measurements for each mass. This is done by (a) extracting all baseline measurements, (b) calculating a sliding window mean and standard error, (c) interpolating over the entire measurement session and (d) applying the mean and SE values at t_0 for each sample. This is similar to how *lolite* (Paton *et al.* 2011) treats background subtraction and results in slightly smaller random uncertainties for individual analyses.

Aside from how data are extracted from time-series measurements and how the background calculations are treated, the data reduction software, *AgeCalcML*, employs methods of the original *AgeCalc* (Gehrels *et al.* 2008). Background measurements are calculated as the mean SE,

$$SE_{\text{background}} = \frac{1}{\sqrt{n}} \sqrt{\frac{\sum_{i=1}^n (x_i - \text{mean}(x))^2}{n-1}} \quad (1)$$

where x is one of seven measured isotopes and n = the number of individual measurements on background (fifty indexes for 120 analyses h⁻¹) or combined background measurements (forty-eight indexes for 300 analyses h⁻¹; fifty indexes for 600 and 1200 analyses h⁻¹). Mean background measurements are subtracted from each individual measurement (i.e., each index):

$$BLS = x_i - \text{mean}(\text{background}) \quad (2)$$

Calculation of ²⁰⁴Pb from isobaric interference of ²⁰⁴(Hg + Pb) is done by subtracting the ²⁰⁴Hg contribution based on the stable ratio of ²⁰⁴Hg/²⁰²Hg of 4.35 (Zadnik *et al.* 1989):

$$^{204}\text{Pb} = ^{204}(\text{Hg} + \text{Pb}) - \frac{^{202}\text{Hg}}{4.35} \quad (3)$$

Following background subtraction, isotopic ratios are calculated for each index; ²⁰⁶Pb/²⁰⁷Pb ratios < 1.81818 and > 21.71787 are discarded, as the former yield dates older than the Earth and the latter yield dates into the future.

Due to the short on-peak durations in acquisition rates of 300–1200 analyses h⁻¹, only the 120 analyses h⁻¹ method incorporates a down-hole fractionation correction for

²⁰⁶Pb/²³⁸U and ²⁰⁸Pb/²³²Th (Košler and Sylvester 2003). This correction is calculated via linear regression of ²⁰⁶Pb/²³⁸U and ²⁰⁸Pb/²³²Th values from 1 s (five indexes) after the start of ablation, resulting in seventy individual measurements from which linear regression is calculated and projected to the first index.

The uncertainty of each analysis for the 120 analyses h⁻¹ acquisition rate depends on down-hole fractionation. This is calculated by first computing the covariance matrix for the seventy on-peak index measurements:

$$\Sigma = \text{MSE}(X'X)^{-1} \quad (4)$$

Then, SE of the linear fit is calculated as

$$\text{SE on peak} = \text{diag}(\sqrt{\Sigma}) \quad (5)$$

Uncertainties for 300–1200 analyses h⁻¹ are calculated differently. Ratios are obtained using a ‘total counts’ method, which eliminates the need for down-hole correction given sufficiently short ablation times (e.g., Johnston *et al.* 2009):

$$z = \frac{\sum_{i=1}^n x_i}{\sum_{i=1}^n y_i} \quad (6)$$

where x and y are individual isotopic measurements and z is the ratio of interest (e.g., ²⁰⁶Pb/²³⁸U). The SE for on-peak uncertainties is calculated based on ratios:

$$\text{SE on peak} = \frac{1}{\sqrt{n}} \sqrt{\frac{\sum_{i=1}^n \left(\frac{x_i}{y_i} - \text{mean}\left(\frac{x_i}{y_i}\right) \right)^2}{n-1}} \quad (7)$$

x and y represent isotopes of interest.

After individual analyses are parsed from each isotopic mass time-series measurement, background measurements subtracted, and the ratios of interest with their corresponding uncertainties are calculated, each analysis is matched to its corresponding sample name from the automated laser schedule generated in the laser software.

Fractionation due to mass spectrometer instrumental drift, mass bias and laser-induced fractionation is calculated by bracketing five unknown analyses to one primary reference analysis. We used zircon FC-1 from the Duluth gabbro with an accepted age of 1099.0 ± 0.6 Ma (Paces and Miller 1993) as our primary reference material for several reasons: (a) it displays remarkably consistent ²⁰⁶Pb/²³⁸U and ²⁰⁶Pb/²⁰⁷Pb values; (b) it yields consistent isotopic ratios when calculated using down-hole regression and total

counts; and (c) it displays a less aggressive (shallower time vs. $^{206}\text{Pb}/^{238}\text{U}$ slope) down-hole fractionation than other commonly used reference materials. The $^{206}\text{Pb}/^{238}\text{U}$ and $^{206}\text{Pb}/^{207}\text{Pb}$ fractionation factors ($FF68$ and $FF67$) for FC-1 are calculated as

$$FF68 = \frac{FC68_{\text{accepted}}}{BLS68_{\text{measured}} \times \left(\frac{(BLS64_{\text{measured}} \times \text{Factor}_{64}) - FC64_c}{BLS64_{\text{measured}} \times \text{Factor}_{64}} \right)} \quad (8)$$

and

$$FF67 = \frac{FC67_{\text{accepted}}}{\left(\frac{(BLS64_{\text{measured}} \times \text{Factor}_{64}) - FC64_c}{\left(\frac{BLS64_{\text{measured}} \times \text{Factor}_{64}}{BLS67_{\text{measured}}} \right) - FC67_c} \right)} \quad (9)$$

where BLS is the measured and background subtracted $^{206}\text{Pb}/^{238}\text{U}$ and $^{206}\text{Pb}/^{204}\text{Pb}$ on-peak values. $FC68_{\text{accepted}}$, $FC67_{\text{accepted}}$, $FC64_c$ and $FC67_c$ are FC-1 values reported in Paces and Miller (1993); Factor_{64} is a user-defined parameter that controls the severity of the common Pb correction with higher values corresponding to a less aggressive correction (see below). Fractionation factor outliers are rejected based on a cut-off percent deviation from the median measured $FF68$ and $FF67$; in this study, we applied conservative filters set to 3% for $FF68$ and 10% for $FF67$ to remove only egregious outliers. Fractionation factor mean and uncertainty are calculated using a sliding window over thirty measurements, which incorporates one primary reference measurement to every five unknown zircon measurement.

All results are common Pb-corrected based on polynomial regression of Pb compositions presented in Stacey and Kramers (1975, their table 6):

$$\alpha = \frac{\log(FF68 \times BLS68_{\text{measured}} + 1)}{0.000155125} \quad (10)$$

$$\beta = 18.761 - 0.0000001 \times \alpha^2 - 0.0016 \times \alpha \quad (11)$$

and

$$\gamma = 15.671 - 0.0000000009 \times \alpha^3 + 0.0000002 \times \alpha^2 - 0.0003 \times \alpha \quad (12)$$

which is applied to $^{206}\text{Pb}/^{238}\text{U}$ measurements as

$$BLS68_{\text{pbc}} = (BLS68_{\text{measured}} \times BLS68_{\text{sw}}) \times \left(\frac{(BLS64 \times \text{Factor}_{64}) - \beta}{BLS64_{\text{measured}} \times \text{Factor}_{64}} \right) \quad (13)$$

Final $^{206}\text{Pb}/^{207}\text{Pb}$ ratios are calculated as

Ratio67

$$= BLS67_{\text{measured}} \times \left(\frac{(BLS64_{\text{measured}} \times \text{Factor}_{64}) - \beta}{BLS64_{\text{measured}} \times \text{Factor}_{64}} \right) \frac{1}{BLS67_{\text{measured}} - \gamma} \quad (14)$$

$^{206}\text{Pb}/^{238}\text{U}$ and $^{207}\text{Pb}/^{235}\text{U}$ ratio calculations require correction in order to output U and Th parts per million (ppm). Counts per second (cps) are determined from Faraday data by multiplying corrected voltage measurements by 80000000 (for $3 \times 10^{11} \Omega$ resistors on a Nu plasma high-resolution HR multi-collector). Results are corrected to FC-1 by taking the mean ^{238}U and ^{232}Th for all primary reference analyses during the measurement session:

$$^{238}\text{U}_{\text{ppm}} = \frac{^{238}\text{U}_{\text{cps}} \times FC_{\text{ppmU}}}{\text{mean}(^{238}\text{U}_{\text{cps}} \text{ session})} \quad (15)$$

and

$$^{232}\text{Th}_{\text{ppm}} = \frac{^{232}\text{Th}_{\text{cps}} \times FC_{\text{ppmTh}}}{\text{mean}(^{232}\text{Th}_{\text{cps}} \text{ session})} \quad (16)$$

where FC_{ppmU} and FC_{ppmTh} are values reported in Paces and Miller (1993). Measured U/Th is calculated as

$$\text{UTh}_{\text{measured}} = \frac{^{238}\text{U}_{\text{ppm}}}{^{232}\text{Th}_{\text{ppm}}} \quad (17)$$

Final $^{206}\text{Pb}/^{238}\text{U}$ isotopic ratios are then calculated as

$$\text{Ratio68} = BLS68_{\text{pbc}} - \left[\frac{0.000000000155}{0.0000092} \times \left(\frac{1}{\frac{\text{UTh}_{\text{measured}}}{2.3} - 1} \right) \right] \quad (18)$$

The value 2.3 is the assumed Th/U magma composition (e.g., Crowley *et al.* 2007). The $^{207}\text{Pb}/^{235}\text{U}$ ratios are calculated using the currently accepted value for $^{238}\text{U}/^{235}\text{U}$ of 137.818 ± 0.045 (Hiess *et al.* 2012):

$$\text{Ratio75} = \frac{\text{Ratio68}}{\text{Ratio67}} \times 137.818 \quad (19)$$

Random measurement uncertainties for on-peak, background and fractionation measurements are propagated in quadrature as:

Table 2.
Zircon reference materials

Reference material	$^{206}\text{Pb}/^{238}\text{U}$ age (Ma, $\pm 2s$)	$^{206}\text{Pb}/^{207}\text{Pb}$ age (Ma, $\pm 2s$)	Technique	Publication for date
Fish Canyon	28.478 \pm 0.024	NA	ID-TIMS	Schmitz and Bowring (2001)
Fish Canyon	28.61 \pm 0.08	NA	CA-ID-TIMS	Bachmann and Charlier (2007)
GHR1	48.106 \pm 0.023 Ma	NA	ID-TIMS	Eddy <i>et al.</i> (2019)
Plesovice	337.16 \pm 0.11 Ma	337.96 \pm 0.61 Ma	ID-TIMS	Sláma <i>et al.</i> (2008)
Plesovice	337.1 \pm 0.2 Ma	339.3 \pm 0.3 Ma	ID-TIMS	Sláma <i>et al.</i> (2008) ^a
Temora-2	416.78 \pm 0.33 Ma	NA	ID-TIMS	Black <i>et al.</i> (2004)
Temora-2	418.37 \pm 0.14 Ma	420.13 \pm 0.30 Ma	CA-ID-TIMS	Mattinson (2010)
R33	419.3 \pm 0.4 Ma	NA	ID-TIMS	Black <i>et al.</i> (2004)
R33	420.53 \pm 0.16 Ma	422.37 \pm 0.36 Ma	CA-ID-TIMS	Mattinson (2010)
Sri Lanka 2	563.2 \pm 4.8 Ma	568 \pm 16 Ma	ID-TIMS	Gehrels <i>et al.</i> (2008)
Peixe	564 \pm 4 Ma	564 \pm 4 Ma	ID-TIMS	Chang <i>et al.</i> (2006)
91500	1062.4 \pm 1.9 Ma	1065.4 \pm 0.5 Ma	ID-TIMS	Wiedenbeck <i>et al.</i> (1995, 2004)
91500	1063.51 \pm 0.39 Ma	1066.0 \pm 0.6 Ma	ID-TIMS	Wiedenbeck <i>et al.</i> (1995, 2004) ^a
91500	1063.6 \pm 1.4 Ma	1066.4 \pm 5.0 Ma	ID-TIMS	Schoene <i>et al.</i> (2006)
FC-1	1099.5 \pm 0.5 Ma	1099.0 \pm 0.6 Ma	ID-TIMS	Paces and Miller (1993)
FC-1	1095.32 \pm 0.33 Ma	1098.47 \pm 0.16 Ma	CA-ID-TIMS	Mattinson (2010)
Oracle	1436.2 \pm 1.3 Ma	1437.05 \pm 0.77 Ma	CA-ID-TIMS	S. Bowring (written communication)
QGNG	1842.0 \pm 3.1 Ma	1851.6 \pm 0.6 Ma	ID-TIMS	Black <i>et al.</i> (2004)
QGNG	1848.7 \pm 2.7 Ma	1851.5 \pm 5.8 Ma	CA-ID-TIMS	Schoene <i>et al.</i> (2006)
Tan Brown	2507.8 \pm 1.5 Ma	2512.24 \pm 0.71 Ma	ID-TIMS	Bauer <i>et al.</i> (2020)
Tan Brown	2508.9 \pm 1.2 Ma	2511.95 \pm 0.86 Ma	CA-ID-TIMS	Bauer <i>et al.</i> (2020)
OG-1	3440.7 \pm 3.2 Ma	3465.4 \pm 0.6 Ma	ID-TIMS	Stern <i>et al.</i> (2009)
OG-1	3463.3 \pm 3.6 Ma	3467.1 \pm 0.6 Ma	CA-ID-TIMS	Bodorkos <i>et al.</i> (2009)

Table data sourced from the Arizona LaserChron Center website, laserchron.org.

^a Recalculated by Horstwood *et al.* (2016).

$$SE_{\text{total}} = \sqrt{SE_{\text{onpeak}}^2 + SE_{\text{background}}^2 + SE_{\text{fractionation}}^2 + SE_{\text{BLS64measured}}^2} \quad (20)$$

Systematic uncertainties are calculated based on primary reference analyses by adding SE from the sliding window, common Pb correction and decay constants as

$$SE_{68\text{systematic}} = \sqrt{\frac{FFSE_{68}^2}{BLS_{68sw}^2} + BLS_{68}pb c^2 + 0.053^2 + 0.035^2} \quad (21)$$

and

$$SE_{67\text{systematic}} = \sqrt{\frac{FFSE_{67}^2}{BLS_{67sw}^2} + BLS_{67}pb c^2 + 0.053^2 + 0.069^2 + 0.035^2} \quad (22)$$

and are reported as 2s. Systematic uncertainties typically result in an additional 1% for $^{206}\text{Pb}/^{207}\text{Pb}$ and $^{206}\text{Pb}/^{238}\text{U}$.

Systematic uncertainties are not included in the uncertainty propagation for each individual analysis. However, systematic uncertainties should be propagated in quadrature with the reported random uncertainties when comparing individual analyses from separate measurement sessions, or after calculating a weighted mean (Horstwood *et al.* 2016).

Results are quality-controlled with user-defined options and filters in *AgeCalcML*. These include $^{206}\text{Pb}/^{207}\text{Pb}$ and $^{206}\text{Pb}/^{238}\text{U}$ best age cut-offs; $^{206}\text{Pb}/^{207}\text{Pb}$ and $^{206}\text{Pb}/^{238}\text{U}$ uncertainty thresholds; positive discordance filter and application age specification; reverse discordance filter applied to all dates; ^{204}Pb filter and $^{206}\text{Pb}/^{204}\text{Pb}$ factor; and over-dispersion factor. For results presented below, we applied uncertainty cut-offs of 10%, a discordance filter of 10% applied to best ages > 600 Ma, a reverse discordance filter of 5%, a ^{204}Pb filter of 400 cps and a variety of $^{206}\text{Pb}/^{204}\text{Pb}$ factors depending on the measurement session (see Appendix S1). Best ages were assigned using a transition of 1200 Ma for efficacy testing and 900 Ma from the detrital application. Over-dispersion factor was set to 1 (i.e., no over-dispersion correction).

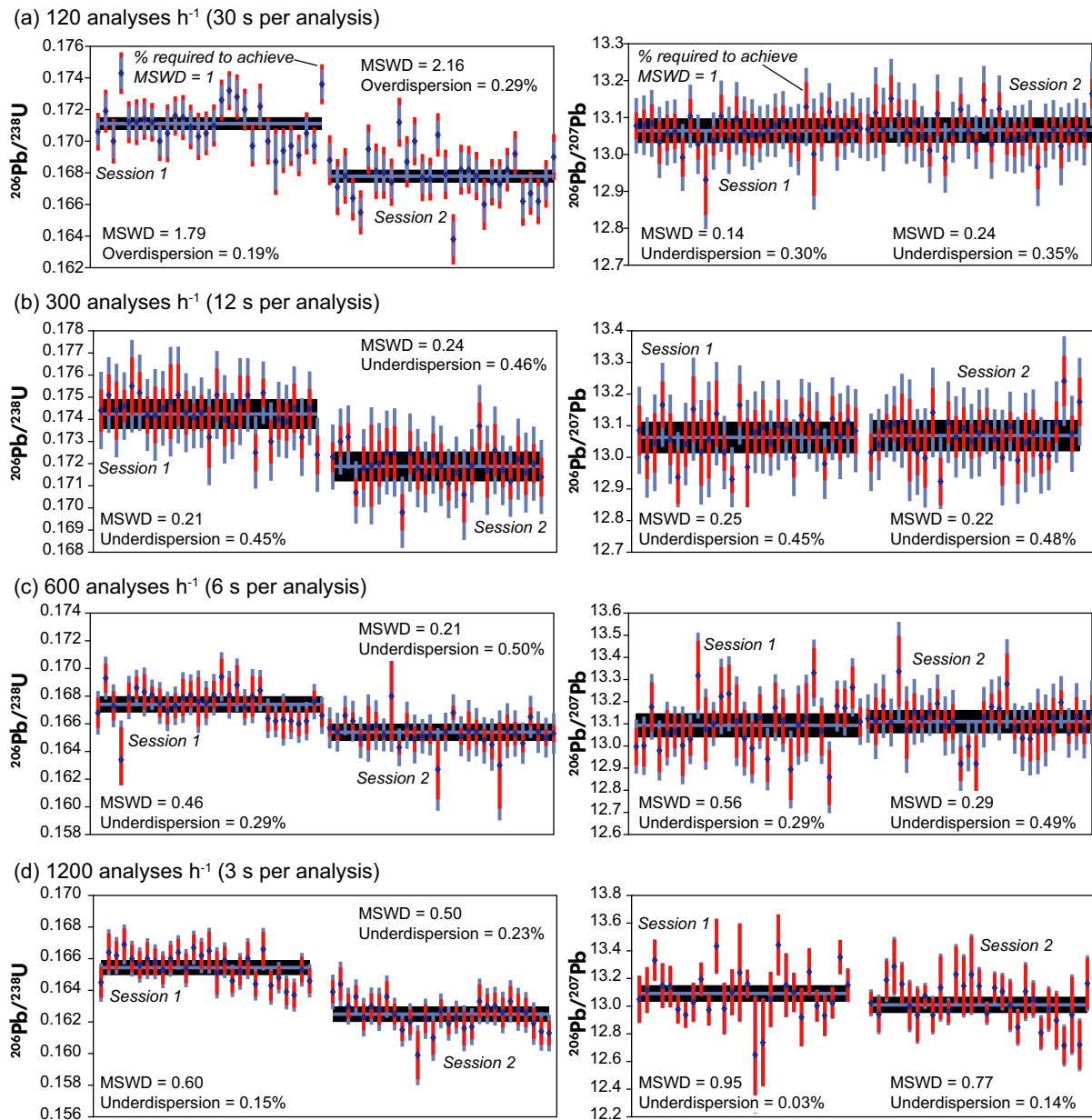


Figure 4. Primary reference material FC-1 for the four rates of data acquisition: (a) 120 analyses h⁻¹ (30 s per analysis), (b) 300 analyses h⁻¹ (12 s per analysis), (c) 600 analyses h⁻¹ (6 s per analysis) and (d) 1200 analyses h⁻¹ (3 s per analysis) with random uncertainties plotted at 1 s. Blue vertical lines are measured ratios and uncertainties for ²⁰⁶Pb/²³⁸U (left panel) and ²⁰⁶Pb/²⁰⁷Pb (right panel). Red vertical lines represent uncertainty (at 1 s) adjustment required to achieve MSWD = 1; over-dispersed results (MSWD > 1) require additional uncertainty (at 1 s) and under-dispersed results (MSWD < 1) require reduced uncertainty. Most results for the four methods are under-dispersed. Results are from two separate sessions run on 19 and 20 April 2019. Black horizontal lines with grey shading are weighted means with 2s uncertainty. Ratios are only background subtracted raw measurements (not fractionation corrected) and include uncertainties from measured ratios and background subtraction.

Efficacy testing

We analysed twelve commonly used zircon reference materials characterised by conventional ID-TIMS and chemical

abrasion (CA) ID-TIMS. The ages of the reference materials range from ~ 3465 to ~ 28 Ma (Table 2). We relied on ID-TIMS dates rather than CA-ID-TIMS where possible because the grains we analysed by LA-ICP-MS were not chemically

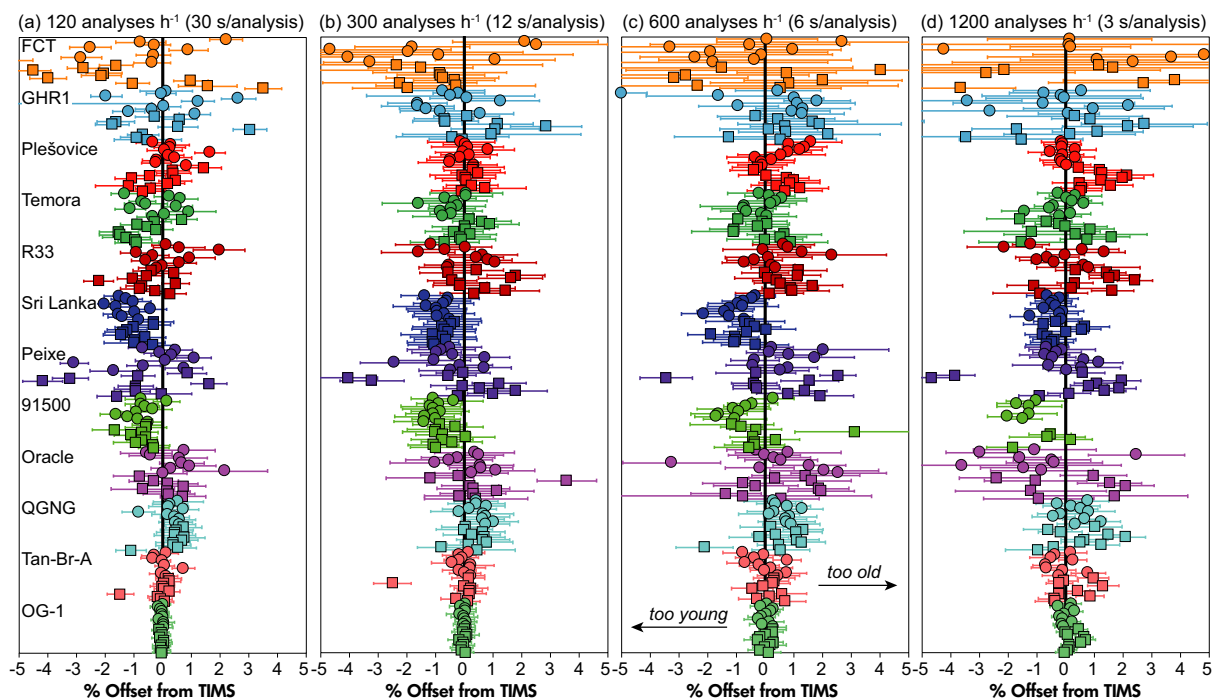


Figure 5. Age offset plots. Circles = Session 1 (runs 1–4) on 19 April 2019. Squares = Session 2 (runs 5–8) on 20 April 2019. (a) 120 analyses h^{-1} (30 s per analyses) includes down-hole correction; all other methods are calculated with total counts. (b) 300 analyses h^{-1} (12 s per analysis). (c) 600 analyses h^{-1} (6 s per analysis). (d) 1200 analyses h^{-1} (3 s per analysis). Offset was calculated as measured date – ID-TIMS date; left of 0% is young offset and right of 0% is old offset. Dates < 1200 Ma are $^{206}Pb/^{238}U$, and ages > 1200 Ma are $^{206}Pb/^{207}Pb$. Random uncertainties are 1 s.

abraded. Ten zircon grains from each of the twelve reference materials were analysed in two separate measurement sessions, treating all analyses as unknowns for comparison with accepted high-precision dates.

Primary reference material uncertainties appropriately represent the dispersion in the data. Specifically, $^{206}Pb/^{238}U$ and $^{206}Pb/^{207}Pb$ uncertainties propagated for each method yielded a mean square weighted deviation (MSWD) close to 1, the sample size-dependent value in which the uncertainties are within the observed data dispersion (Wendt and Carl 1991). For each session, we calculated the amount of uncertainty required to be added or subtracted to force MSWD to equal 1 (vertical red bars and inset per cent values in Figure 4). Only $^{206}Pb/^{238}U$ of the 120 analyses per hour rate proved over-dispersed with MSWD > 1, which required 0.19–0.29% (1s) additional uncertainty to achieve MSWD = 1 (Figure 4a, left). As there is less dispersion in these results compared with faster rates of acquisition, this means the uncertainties are slightly underestimated, which is commonly corrected using an over-dispersion factor (e.g., Gehrels *et al.* 2008), and can optionally be done in *AgeCalcML*. All other primary

reference material measurements yielded under-dispersed (overestimated uncertainty relative to the data dispersion) results with MSWD < 1. The 120 analyses h^{-1} acquisition rate required 0.30–0.35% less $^{206}Pb/^{207}Pb$ uncertainty to achieve a MSWD of 1 (Figure 4a, right). For the 300–1200 analyses h^{-1} acquisition rates, low MSWD values systematically increased with faster acquisition rates (Figure 4b–d). Rates of 300, 600 and 1200 analyses h^{-1} required 0.45–0.46%, 0.29–0.50% and 0.15–0.23% (1s) less $^{206}Pb/^{238}U$ uncertainty, and 0.45–0.48%, 0.29–0.49% and 0.03–0.14% (1s) less $^{206}Pb/^{207}Pb$ uncertainty to achieve a MSWD value of 1, respectively (Figure 4b–d). Although it is always a compromise between dispersion and ascribed uncertainty, this increase in MSWD from 300 to 1200 analyses h^{-1} appears to be largely controlled by the amount of data dispersion, as shorter on-peak measurement times would naturally yield a higher dispersion for individual analyses (Figure 4b–d).

Whether or not uncertainty contributions from over-dispersion and under-dispersion should be systematically added or subtracted to unknown analyses based on the primary reference material behaviour remains an open

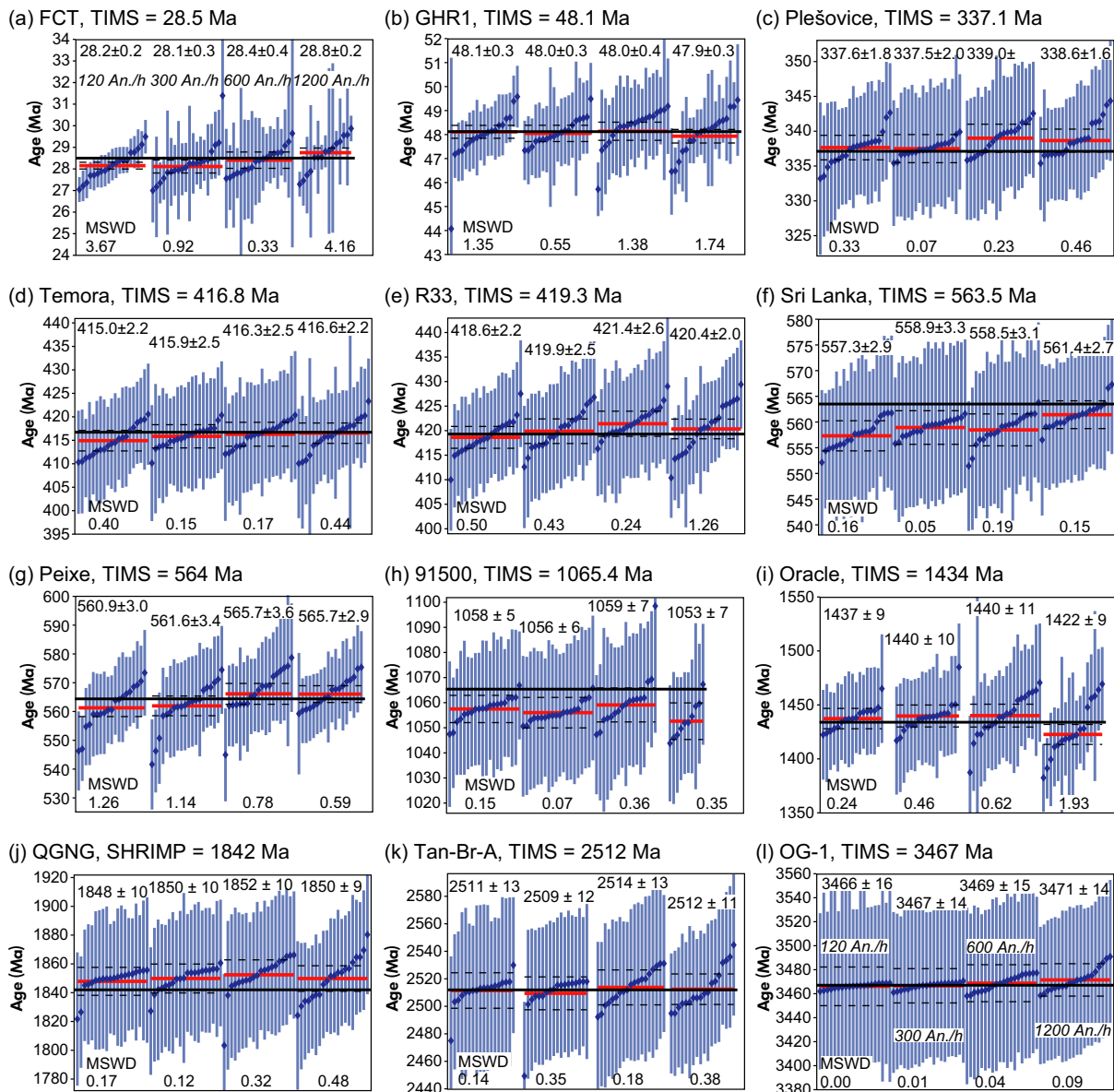


Figure 6. Weighted mean plots. Four groups in each plot from left to right are the four rates of data acquisition: 120 analyses h^{-1} (30 s per analysis), 300 analyses h^{-1} (12 s per analysis), 600 analyses h^{-1} (6 s per analysis) and 1200 analyses h^{-1} (3 s per analysis). Blue vertical lines are calculated, and pooled dates from both measurement sessions run on 19 and 20 April 2019. (a–h) are dates and uncertainties calculated using $^{206}\text{Pb}/^{238}\text{U}$; (i–l) are dates and uncertainties using $^{206}\text{Pb}/^{207}\text{Pb}$. Systematic uncertainties are included from each separate measurement session. Black horizontal lines with grey shading are 2s uncertainty. An. = analyses.

question. Doing so requires the assumption that both primary reference materials and unknowns exhibit equal behaviours that result in data dispersion due to variations in ablation characteristics, isotopic fractionation and matrix effects, which is rarely the case. For this reason, we did not add over- and under-dispersion factors for any of the analytical results presented in this study, although we incorporated the option to do so in *AgeCalcML*.

Residual offsets calculated based on subtracting the measured dates from accepted high-precision ID-TIMS dates yielded either slightly positive (too old) or slightly negative (too young) results (Figure 5). Offset plots in Figure 5 reveal many interesting observations. First, most analysed zircons are within 5% of high-precision dates regardless of acquisition rate, and the overwhelming majority are within 2%. Second, the uncertainty in individual

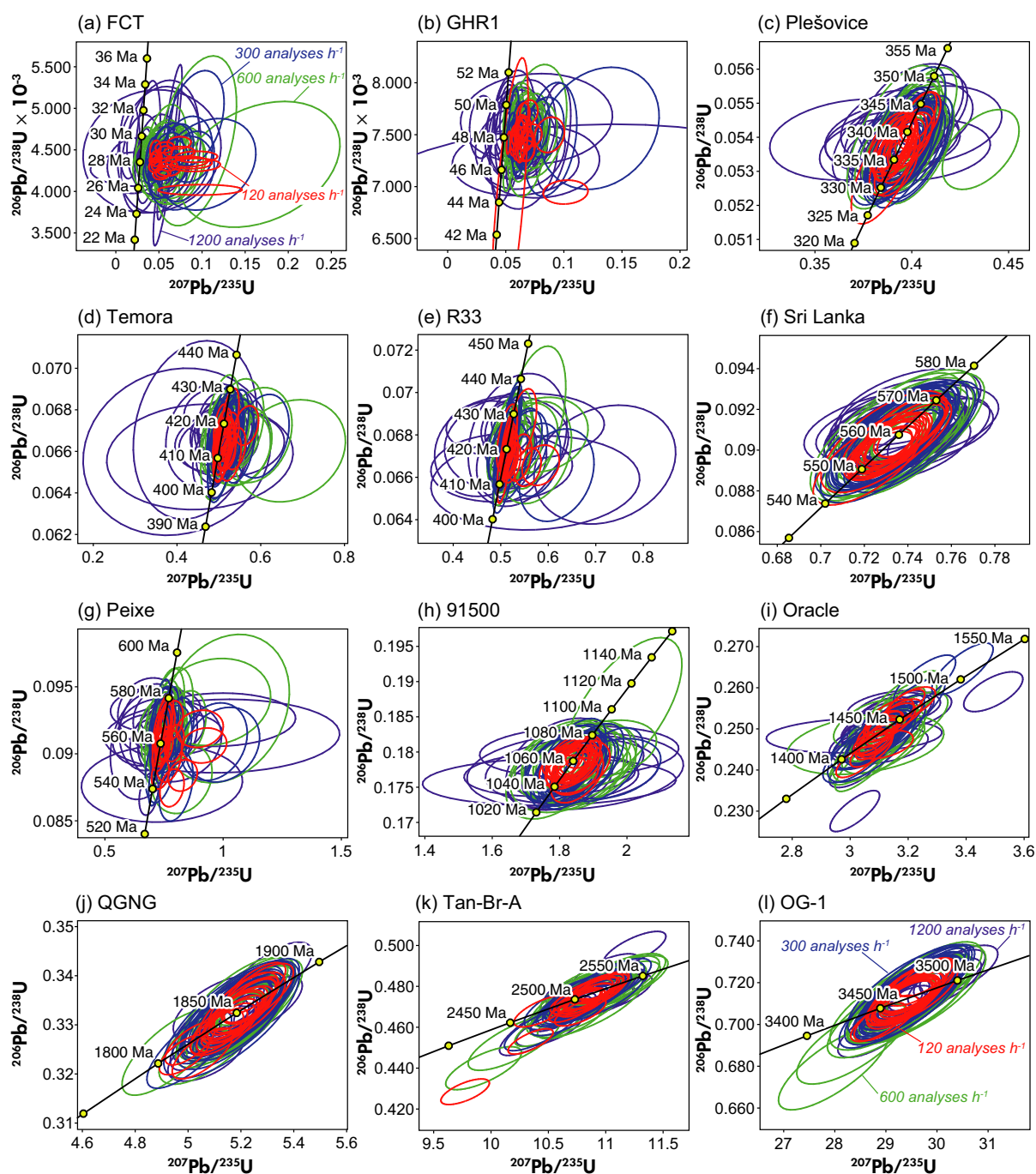


Figure 7. Concordia diagrams. Purple ellipses are 1200 analyses h^{-1} (3 s per analysis). Green ellipses are 600 analyses h^{-1} (6 s per analysis). Blue ellipses are 300 analyses h^{-1} (12 s per analysis). Red ellipses are 120 analyses h^{-1} (30 s per analysis). All uncertainty ellipses represent 2s. See Table 2 for reference material information. Note that the young reference materials (FCT and GHR1) are slightly positively discordant. This is because a compromise has to be made in the common Pb correction. Specifically, all panels in this figure share the same concordia line, and forcing these young zircons concordant by increasing the severity of the common Pb correction by decreasing *Factor64* (see Data reduction section) results in positively discordant older reference materials (e.g., Tan-Br-A and OG1).

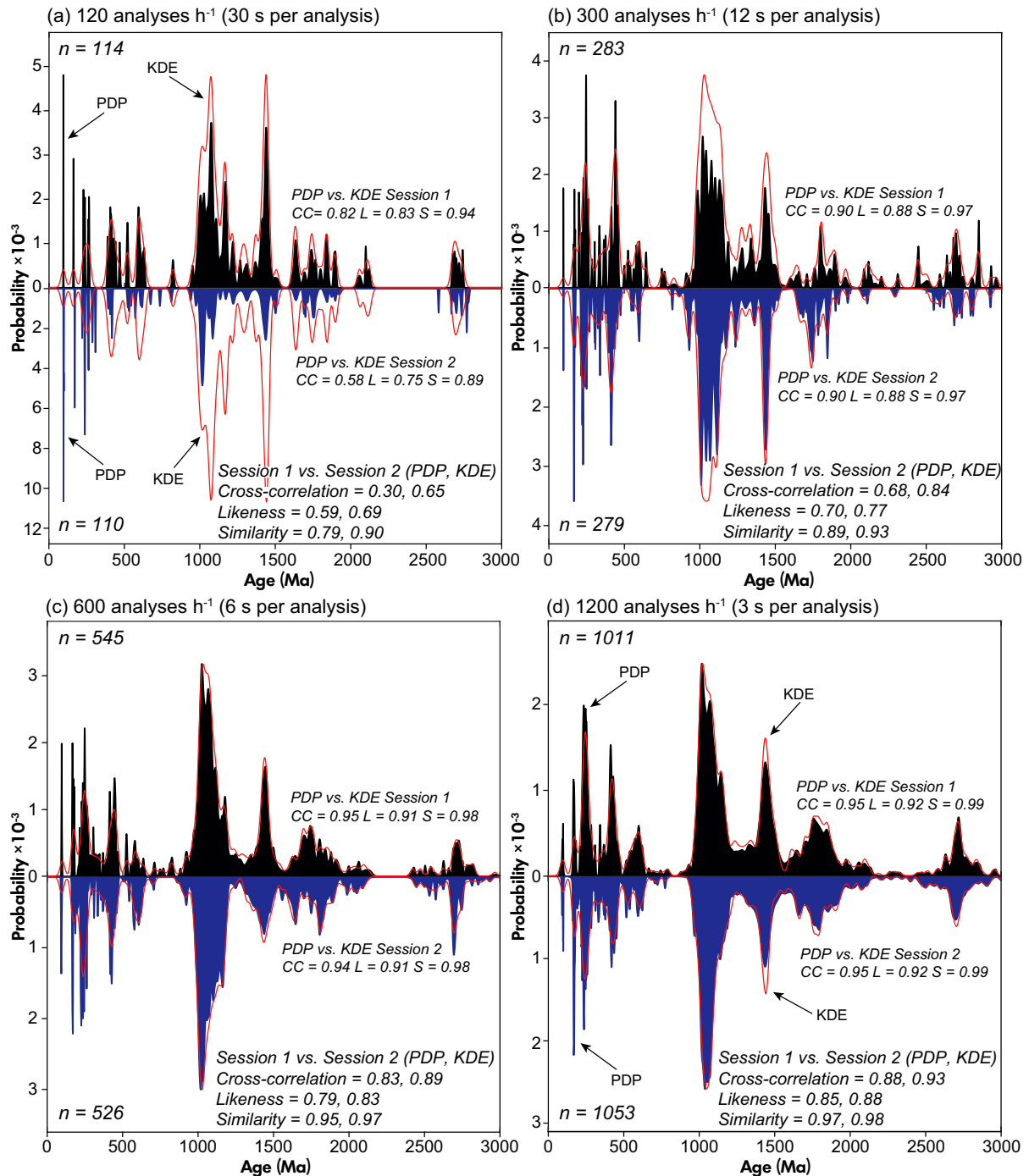


Figure 8. Results for detrital sample CP40 (Dickinson and Gehrels 2008). Age distributions for eight separate measurement sessions. The same number of zircons was analysed at each rate (i.e., 120 unknowns were analysed at 120 analyses h^{-1} ; 300 unknowns were analysed at 300 analyses h^{-1}). Y-axis probability corresponds only to probability density plots (PDP). Kernel density estimates (KDEs) were constructed using a 15 My bandwidth. CC = cross-correlation. L = likeness. S = similarity. All quantitative comparisons were calculated using *DZstats* (Saylor and Sundell 2016) version 2.3 for MacOS.

dates show a systematic decrease from fast to slow acquisition rates and young to old dates; an expected reality as the former is a result of fewer total ions counted

during faster acquisitions, and the latter is a result of better reproducibility and precision afforded by $^{206}\text{Pb}/^{207}\text{Pb}$ determination. Third, results show systematic offsets for

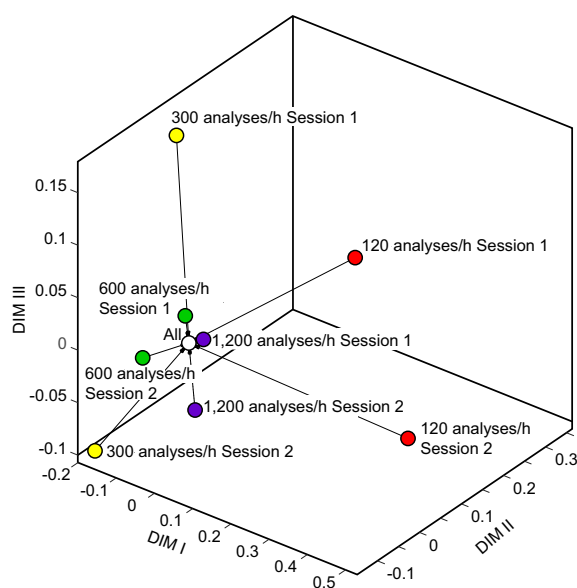


Figure 9. Three-dimensional multidimensional scaling (MDS) plot of results from the detrital application (see Detrital application section). Red circles = 120 analyses h^{-1} ; blue circles = 300 analyses h^{-1} ; green circles = 600 analyses h^{-1} ; purple circles = 1200 analyses h^{-1} ; white circle = all accepted dates produced in this study. Black arrows correspond to the nearest neighbour. The comparison metric used is 1 – cross-correlation of kernel density estimates (KDEs) with a 15 My bandwidth to produce dissimilarity measure used to produce the MDS plot.

reference materials regardless of acquisition rate; that is, too old and too young dates at 120 analyses h^{-1} typically show the same behaviour at faster acquisition rates (compare QGNG for all four methods in Figure 5). Fourth, in some cases the results are better in the fast acquisition (compare Sri Lanka for all four methods in Figure 5 where the 1200 analyses h^{-1} clearly outperforms the other acquisition rates). This latter observation is particularly interesting because the subtle variability and minor offsets among methods point to session-specific dispersion and/or instrument drift in the fractionation correction rather than significant issues with the faster acquisition methods. Furthermore, variations in down-hole fractionation and compositional heterogeneity are expected to become less important with shorter acquisition rates, which may also contribute to better analytical results in some cases.

Weighted mean calculations including systematic uncertainties (see Data reduction section) for the twelve reference materials show similar systematic offsets to accepted high-

precision ID-TIMS dates for the four different acquisition rates (Figure 6). For example, Sri Lanka zircon is systematically too young, whereas QGNG is systematically too old for all four methods.

Concordia diagrams provide an informative way to interrogate variability based on acquisition rate (Figure 7). In some cases, variability in the acquisition session results in more dispersion at slower rates of acquisition. For example, 600 analyses h^{-1} shows more dispersion than 1200 analyses h^{-1} for the oldest reference materials (Figure 7k–l). Young dates (e.g., FCT) are positively discordant because the common Pb correction is applied to the entire acquisition session. These young dates could be forced onto the concordia line by applying a lower *Factor64* (see previous section), but this results in positively discordant older dates, as a lower *Factor64* results in a more aggressive application of the Stacey and Kramers (1975) common Pb correction (see Data reduction section, $^{206}Pb/^{204}Pb$ factor).

The number of rejected analyses for the reference material testing sessions generally increases with faster acquisition rate. For this study, a total of 240 reference materials were analysed at each rate (twelve zircons analysed ten times for two measurement sessions). The number of rejected analyses results from filtering of the data (see previous section). At 120 analyses h^{-1} , three out of the 240 individual analyses were rejected (~ 1%). At 300 analyses h^{-1} , six analyses were rejected (~ 3%). At 600 analyses h^{-1} , five analyses were rejected (~ 2%). At 1200 analyses h^{-1} , sixteen out of 240 were rejected (~ 7%). For the latter, fourteen of the sixteen rejected were for reference materials FCT and 91500, with the former all rejected due to high $^{206}Pb/^{238}U$ uncertainty and the latter due to reverse discordance, both likely resulting from low radiogenic ^{206}Pb and ^{207}Pb , respectively.

Detrital application

To demonstrate the utility of the new rapid U-Pb acquisition methods, we investigated the previously characterised large-*n* sample from Pullen *et al.* (2014), CP40, originally reported in Dickinson and Gehrels (2008). CP40 is a fluvial arenite sample from the Upper Cretaceous Wahweap Formation near Henrieville Creek, Utah (Dickinson and Gehrels 2008). We chose CP40 for this study because (a) it was previously characterised by large-*n* U-Pb geochronology using two separate methods (single- and multi-collector LA-ICP-MS, Pullen *et al.* 2014) and (b) it contains approximately fourteen discernible age peaks, of which the youngest approximates the depositional age. To limit sample bias in our test of the new rapid acquisition

methods, we mounted CP40 unknown zircons with primary and secondary reference materials (FC-1 and R33, respectively) on a single epoxy mount from which we randomly assigned spots for each test. In total, we conducted eight individual measurement sessions: four tests for each acquisition rate, two sessions each. For each test, we analysed the same number of unknowns as the acquisition rate itself to test how many dates could be acquired in a given amount of time, and how much the resulting age distributions vary. For example, we analysed 120 unknowns at a rate of 120 analyses h^{-1} and 300 unknowns at a rate of 300 analyses h^{-1} .

Qualitative results show a dramatic increase in correspondence (similarity) with larger sample sizes afforded by the faster 600 and 1200 analyses h^{-1} acquisition rates. This is the case for comparison of different sessions and age distribution types in the same session (Figure 8). Specifically, results plotted as probability density plots (PDPs) and kernel density estimates (KDEs) show increased correspondence between the two sessions and a convergence in the number of age populations. The major increase in correspondence appears to be between results from 300 and 600 analyses h^{-1} sessions (Figures 8 and 9).

Quantitative comparisons are consistent with qualitative assessments. Quantitative comparison of PDPs and KDEs was conducted using three measures of correspondence: Cross-correlation (Saylor *et al.* 2012), Likeness (Satkoski *et al.* 2013) and Similarity (Gehrels 2000) calculated using *DZstats* (Saylor and Sundell 2016) version 2.3 for MacOS. All inter-session comparisons of Session 1 and Session 2 show an increase in correspondence with increased n . Specifically, Cross-correlation, Likeness and Similarity of PDPs increases from 0.30, 0.59 and 0.79 for age distributions gathered at 120 analyses h^{-1} to much consistently higher values of 0.88, 0.85 and 0.97 for age distributions gathered at 1200 analyses h^{-1} . Similarly, quantitative comparisons of KDEs increase from 0.65, 0.69 and 0.90 for age distributions gathered at 120 analyses h^{-1} to 0.93, 0.88 and 0.98 for age distributions gathered at 1200 analyses h^{-1} (Session 1 vs. Session 2 in Figure 8).

PDPs and KDEs are less distinguishable with increased n . Quantitative intra-session comparisons of PDPs and KDEs show consistently increased correspondence with increased n . Session 1 results yielded 0.82, 0.83 and 0.94 for age distributions gathered at 120 analyses h^{-1} to 0.92, 0.95 and 0.99 for age distributions gathered at 1200 analyses h^{-1} . Session 2 results increase from 0.58, 0.75 and 0.89 for age distributions gathered at 120 analyses h^{-1} to 0.92, 0.95 and 0.99 for age distributions gathered at 1200 analyses h^{-1} .

(PDP vs. KDE in Figure 8). This demonstrates that although the uncertainty does increase with faster acquisition rate (Figures 5, 6 and 7) it has little effect on the resulting age distribution, and that larger n age distributions may yield a closer approximation of the parent-age population (which is inherently unknowable).

Multidimensional scaling (MDS) is a useful way to graphically visualise quantitative comparison results by forcing measures of dissimilarity into Cartesian space, with more similar distributions plotting closer together (Vermeesch 2013). Figure 9 shows each session and acquisition rate test (eight total tests) compared with one another and to a distribution comprising all accepted dates produced in this study ($n = 3921$). Results show that distributions characterised by > 300 dates are drastically more similar than distributions with fewer dates and that increased sample size results in a systematic convergence (closeness in MDS space) towards a common underlying age distribution.

The number of accepted vs. rejected analyses for sample CP40 slightly increased with faster acquisition rates. For the two measurement sessions, 5% and 8% were rejected at 120 analyses h^{-1} , 5% and 7% were rejected at 300 analyses h^{-1} , 9% and 12% were rejected at 600 analyses h^{-1} , and 12% and 16% were rejected at 1200 analyses h^{-1} . The majority of the rejected analyses at faster rates is due to low counts of ^{207}Pb resulting in discordance and/or high $^{206}\text{Pb}/^{207}\text{Pb}$ uncertainty, which may result in bias against detrital samples containing young (e.g., Cenozoic) and/or low U zircons (see Appendix S1).

Large- n results yielded significantly more young dates than small- n results (i.e., < 100 Ma) that approximate depositional age. This is important for any study where low abundance dates are important, particularly for studies interested in determining maximum depositional age. The 120 and 300 analyses h^{-1} tests yielded a total of four and two dates < 100 Ma, whereas the 600 and 1200 analyses h^{-1} tests yielded 8 and 13 < 100 Ma dates, respectively. Weighted mean calculations for dates < 100 Ma are 97.0 ± 0.6 Ma (MSWD = 8.1), 96.7 ± 1.5 Ma (MSWD = 0.6), 95.0 ± 0.8 Ma (MSWD = 2.5) and 96.5 ± 1.0 Ma (MSWD = 3.7), respectively.

Discussion

Increased sample throughput and generation of large- n detrital geochronology sample data continue to improve the quality and robustness in sediment provenance research. Large- n samples are especially valuable for quantitative data interpretation methods (e.g., Sundell and

Saylor 2017, Saylor *et al.* 2019) and characterisation of complex age distributions. Results from this study highlight best practices and appropriateness of different acquisition rates that are suited to specific needs based on accuracy, precision and project scope. For example, if the goal is to characterise the detrital zircon U-Pb age distribution of sandstone samples containing abundant Cenozoic grains, then 120 analyses h^{-1} would be the optimal choice. Alternatively, if the goal is to analyse detrital zircons from Mesozoic or older samples, then a faster rate (300–1200 analyses h^{-1}) would be more appropriate depending on the desired resolution of the age populations of interest.

The slowest acquisition rate presented here of 120 analyses h^{-1} most closely represents traditional methods employed in many laser ablation ICP-MS laboratories (Gehrels *et al.* 2006, 2008, Shaulis *et al.* 2010, Horstwood *et al.* 2016) and produces the most robust and reliable data. Slower rates are particularly important for detrital samples containing abundant young (Cenozoic) age populations. Mean random uncertainty for dates < 100 Ma from sample CP40 increases from ± 0.57 My ($\pm 0.58\%$) at 120 analyses h^{-1} to ± 1.0 My ($\pm 1.1\%$) at 300 analyses h^{-1} , ± 1.3 My ($\pm 1.4\%$) at 600 analyses h^{-1} and ± 3.0 My ($\pm 3.2\%$) at 1200 analyses h^{-1} .

For provenance analysis, there is a major improvement in the reproducibility of age distributions with age distributions comprising > 300 dates, which can be rapidly obtained at rates of 300 and 600 analyses h^{-1} with minimal sacrifice in precision and accuracy (Figures 5, 7 and 8). Such age distributions are particularly well-suited for quantitative analysis. Many applications of DZ analysis are centred on questions of presence versus absence of age populations, and thus, rapid acquisition methods of 300–600 analyses h^{-1} hold significant promise for obtaining more representative age distributions without sacrificing data quality.

The fastest acquisition rate presented here of 1200 analyses h^{-1} has significant potential for applications in which low abundance ages are important. For such research it may be critical to search detrital samples for specific, low abundance, but highly informative age groups, such as investigation of the oldest crustal material on Earth hosted in sedimentary rocks of the Jack Hills, Western Australia (e.g., Harrison 2009, Holden *et al.* 2009). Many applications could benefit from minimal damage to individual zircon crystals that it takes to obtain a radiometric date, before application of further geochemical techniques such as Lu-Hf analysis (Gehrels and Pecha 2014), (U-Th)/He thermochronology (Reiners 2005, Stockli 2005), petrochronology by LA-ICP-MS (Kylander-Clark 2017), or high-precision geochronology (Mattinson

2005). Fast acquisition rates also hold promise for DZ studies specifically focused on determining maximum depositional age (i.e., the youngest age or population of ages in a siliciclastic sample); however, debate persists on how best to calculate the maximum depositional age of a sample (Dickinson and Gehrels 2009, Coutts *et al.* 2019). One approach would be to analyse a detrital sample at 1200 analyses h^{-1} in order to identify the youngest grains and reanalyse that age group using a slower (e.g., 120 analyses h^{-1}) rate with multiple analyses for each single grain where possible and/or analyse the grains using high-precision methods (e.g., ID-TIMS) for increased precision and accuracy, thus producing a larger population of the youngest age fraction of the age distribution.

The number of age modes and the gaps and troughs between major age modes decreases with increasing n for the detrital application (Figure 8). This may be the result of increased uncertainty in the faster method; however, this is unlikely because the KDEs (which do not include uncertainties) show the same effect as the PDPs. Alternatively, this might be because larger n results yield better representations of the true (and inherently unknowable) population than the multimodal lower n results, as increased sampling over a wider distribution of ages from these temporally broad age groups results in a smoothing of the age distribution. Smoothing of age distributions could also be the result of spurious ages generated from mixing zones; however, such analyses are typically discordant and/or high uncertainty and are filtered out using standard filtering methods (e.g., Matthews and Guest 2017). This latter point raises a critical issue, in that one of the best ways to avoid such domain mixing and generation of spurious ages is through detailed sample spot selection using a combination of backscatter electron (BSE) and cathodoluminescence (CL) imagery. This increases the sample preparation time, especially with large- n analysis, but can be done away from the mass spectrometer, before the measurement session. Still, if researchers pick spots manually, there is unavoidable bias in sample selection (e.g., based on grain size, shape and colour), and it remains an open question whether this bias outweighs the potential for zone mixing. The ideal situation is sample selection that is automated and incorporates contextual information from BSE and CL imagery; however, such software is currently still under development.

The methods discussed above that enable significantly increased rates of U-Pb age acquisition via LA-ICP-MS require only minor adjustments in LA-ICP-MS hardware and software. The primary hardware requirements are to have a laser ablation system that delivers a very short washout time, a mass spectrometer that has a short integration time and a

multi-collector configuration for efficient counting of ions. The increased rates of acquisition are largely afforded by automation, with software capable of efficiently generating laser schedules (e.g., *Chromium*), and data reduction methods capable of handling time-resolved analysis. The 300, 600 and 1200 analyses h⁻¹ methods require modifications only to data reading, parsing, background subtraction and uncertainty calculation of isotopic ratios; no adjustments to the statistical and mathematical treatment of the data are required following calculation of the isotopic ratios and uncertainty in *AgeCalc* (Gehrels *et al.* 2008) in the new data reduction software contributed here, *AgeCalcML*.

Conclusions and future directions

We present new methods to acquire zircon U-Pb dates at rates of 120 analyses h⁻¹ (30 s per analysis), 300 analyses h⁻¹ (12 s per analysis), 600 analyses h⁻¹ (6 s per analysis) and 1200 analyses h⁻¹ (3 s per analysis) by laser ablation multi-collector ICP-MS. Results based on analysis of twelve zircon reference materials previously characterised by high-precision geochronology show there is little sacrifice in precision and accuracy, and reveal systematic offsets (i.e., too young or too old) compared with ID-TIMS dates. Applying these new analytical routines to a sample of Cretaceous western North America Wahweap Formation (CP40) previously characterised by large-*n* U-Pb analysis reveals a dramatic increase in correspondence (similarity) for age distributions characterised by > 300 dates.

The future of LA-ICP-MS geochronology and geochemistry research is bright. For example, most research has focused on zircon applications, yet there is a growing interest in analysing accessory mineral phases other than zircon such as apatite, baddeleyite, monazite and titanite (Willigers *et al.* 2002, Thomson *et al.* 2012, Ibanez-Mejia *et al.* 2014). The rapid acquisition methods discussed above hold potential for implementation on single-collector ICP-MS instruments (e.g., Pullen *et al.* 2018), and in the acquisition and interpretation of geochronological data in the context of supporting geochemical data for time-resolved interpretations of petrogenetic (rock-forming) processes in the burgeoning field of petrochronology (Kylander-Clark 2017, Kohn and Engi 2019). The rapid acquisition techniques discussed above are particularly useful for sediment provenance research; however, it is never possible to know *a priori* the complexity of a sample. As such, and in consideration of rapid acquisition techniques, it will be critical to develop methods capable of real-time (i.e., during the measurement session) data reduction and visualisation methods. Although this remains a challenge

for time-resolved analysis, it will be important for rapid acquisition methods outlined above, quality control of measurement sessions, and to avoid generating hundreds of dates for detrital samples with simple (unimodal) age distributions. It is also important to consider automated sample spot picking software capable of incorporating BSE and CL imagery to avoid inclusions and complex zoning not visible in reflected light optical imagery and to mitigate inherent bias in manual sample selection.

Acknowledgements

We acknowledge the National Science Foundation (NSF) for continued support of the Arizona LaserChron Center (EAR-1649254) and to the University of Wisconsin for EarthCube Integration: Geochronology Frontier at the Laboratory-Cyberinformatics Interface (EAR-1740694). We thank Nicky Giesler, Marty Pepper and Sarah George at the Arizona LaserChron Center. We also thank Gilby Jepson for testing an *lomite* routine for comparison of results with our new reduction software, *AgeCalcML*. This work benefitted from thoughtful and constructive reviews by two anonymous reviewers and manuscript handling by Editor Paul Sylvester.

Conflict of interest

The authors have no conflicts of interest to declare.

Data availability statement

All data presented in this study are available as part of the online article. Data for CP40 are also archived at Geochron.org.

References

- Andersen T. (2005)**
Detrital zircons as tracers of sedimentary provenance: Limiting conditions from statistics and numerical simulation. *Chemical Geology*, 216, 249–270.
- Bachmann O., Charlier B.L.A. and Lowenstem J.B. (2007)**
Zircon crystallization and recycling in the magma chamber of the rhyolitic Kos Plateau Tuff (Aegean arc). *Geology*, 35, 73–76.



references

- Bauer A.M., Vervoort J.D. and Fisher C.M. (2020)**
Unraveling the complexity of zircons from the 4.0-2.9 Ga Acasta Gneiss Complex. *Geochimica et Cosmochimica Acta*, 283, 85–102.
- Belousova E.A., Griffin W.L., O'Reilly S.Y. and Fisher N.L. (2002)**
Igneous zircon: Trace element composition as an indicator of source rock type. *Contributions to Mineralogy and Petrology*, 143, 602–622.
- Belousova E.A., Kostitsyn Y.A., Griffin W.L., Begg G.C., O'Reilly S.Y. and Pearson N.J. (2010)**
The growth of the continental crust: Constraints from zircon Hf-isotope data. *Lithos*, 119, 457–466.
- Black L.P., Kamo S.L., Allen C.M., Davis D.W., Aleinikoff J.N., Valley J.W., Mundil R., Campbell I.H., Korsch R.J., Williams I.S. and Foudoulis C. (2004)**
Improved $^{206}\text{Pb}/^{238}\text{U}$ microprobe geochronology by the monitoring of a trace-element-related matrix effect; SHRIMP, ID-TIMS, ELA-ICP-MS and oxygen isotope documentation for a series of zircon standards. *Chemical Geology*, 205, 115–140.
- Blum M. and Pecha M. (2014)**
Mid-Cretaceous to Paleocene North American drainage reorganization from detrital zircons. *Geology*, 42, 607–610.
- Bodorkos S., Stern R.A., Kamo S., Corfu F. and Hickman A.H. (2009)**
OG1: A natural reference material for quantifying SIMS instrumental mass fractionation of Pb isotopes during zircon dating. *AGUFM*, 2009, V33B–2044.
- Cawood P.A., Hawkesworth C.J. and Dhuime B. (2012)**
Detrital zircon record and tectonic setting. *Geology*, 40, 875–878.
- Cawood P.A. and Nemchin A.A. (2001)**
Paleogeographic development of the east Laurentian margin: Constraints from U-Pb dating of detrital zircons in the Newfoundland Appalachians. *Geological Society of America Bulletin*, 113, 1234–1246.
- Chang Z., Vervoort J.D., McClelland W.C. and Knaack C. (2006)**
U-Pb dating of zircon by LA-ICP-MS. *Geochemistry Geophysics Geosystems*, 7, 1–14.
- Chemiak D.J., Hanchar J.M. and Watson E.B. (1997)**
Diffusion of tetravalent cations in zircon. *Contributions to Mineralogy and Petrology*, 127, 383–390.
- Chew D., Drost K. and Petrus J.A. (2019)**
Ultrafast, > 50 Hz LA-ICP-MS spot analysis applied to U-Pb dating of zircon and other U-bearing minerals. *Geostandards and Geoanalytical Research*, 43, 39–60.
- Compston W. and Pidgeon R.T. (1986)**
Jack Hills, evidence of more very old detrital zircons in Western Australia. *Nature*, 321, 766–769.
- Cottle J.M., Kylander-Clark A.R. and Vrijmoed J.C. (2012)**
U-Th/Pb geochronology of detrital zircon and monazite by single shot laser ablation inductively coupled plasma-mass spectrometry (SS-LA-ICPMS). *Chemical Geology*, 332, 136–147.
- Cottle J.M., Searle M.P., Horstwood M.S.A. and Waters D.J. (2009)**
Timing of mid-crustal metamorphism, melting, and deformation in the Mount Everest region of southern Tibet revealed by U-(Th)-Pb geochronology. *The Journal of Geology*, 117, 643–664.
- Coutts D.S., Matthews W.A. and Hubbard S.M. (2019)**
Assessment of widely used methods to derive depositional ages from detrital zircon populations. *Geoscience Frontiers*, 10, 1421–1435.
- Crowley J.L., Schoene B. and Bowring S.A. (2007)**
U-Pb dating of zircon in the Bishop Tuff at the millennial scale. *Geology*, 35, 1123–1126.
- Dickinson W.R. and Gehrels G.E. (2008)**
Sediment delivery to the Cordilleran foreland basin: Insights from U-Pb ages of detrital zircons in Upper Jurassic and Cretaceous strata of the Colorado Plateau. *American Journal of Science*, 308, 1041–1082.
- Dickinson W.R. and Gehrels G.E. (2009)**
Use of U-Pb ages of detrital zircons to infer maximum depositional ages of strata: A test against a Colorado Plateau Mesozoic database. *Earth and Planetary Science Letters*, 288, 115–125.
- Dickinson W.R., Lawton T.F. and Gehrels G.E. (2009)**
Recycling detrital zircons: A case study from the Cretaceous Bisbee Group of southern Arizona. *Geology*, 37, 503–506.
- Dodson M.H., Compston W., Williams I.S. and Wilson J.F. (1988)**
A search for ancient detrital zircons in Zimbabwean sediments. *Journal of the Geological Society, London*, 145, 977–983.
- Eddy M.P., Ibañez-Mejía M., Burgess S.D., Coble M.A., Cordani U.G., DesOmeau J., Gehrels G.E., Li X., MacLennan S., Pecha M. and Sato K. (2019)**
GHR 1 zircon – A new Eocene natural reference material for microbeam U-Pb geochronology and Hf isotopic analysis of zircon. *Geostandards and Geoanalytical Research*, 43, 113–132.
- Fedo C.M., Sircombe K.N. and Rainbird R.H. (2003)**
Detrital zircon analysis of the sedimentary record. *Reviews in Mineralogy and Geochemistry*, 53, 277–303.
- Gehrels G.E. (2000)**
Introduction to detrital zircon studies of Paleozoic and Triassic strata in western Nevada and northern California. *Special Paper of the Geological Society of America*, 347, 1–17.
- Gehrels G. (2014)**
Detrital zircon U-Pb geochronology applied to tectonics. *Annual Review of Earth and Planetary Sciences*, 42, 127–149.
- Gehrels G. and Pecha M. (2014)**
Detrital zircon U-Pb geochronology and Hf isotope geochemistry of Paleozoic and Triassic passive margin strata of western North America. *Geosphere*, 10, 49–65.

references

- Gehrels G., Valencia V. and Pullen A. (2006)**
Detrital zircon geochronology by laser-ablation multi-collector ICP-MS at the Arizona LaserChron Center. *The Paleontological Society Papers*, 12, 67–76.
- Gehrels G.E., Valencia V.A. and Ruiz J. (2008)**
Enhanced precision, accuracy, efficiency, and spatial resolution of U-Pb ages by laser ablation-multi-collector-inductively coupled plasma-mass spectrometry. *Geochemistry Geophysics Geosystems*, 9, 1–13.
- Harrison T.M. (2009)**
The Hadean crust: Evidence from > 4 Ga zircons. *Annual Review of Earth and Planetary Sciences*, 37, 479–505.
- Hiess J., Condon D.J., McLean N. and Noble S.R. (2012)**
²³⁸U/²³⁵U systematics in terrestrial uranium-bearing minerals. *Science*, 335, 1610–1614.
- Holden P., Lanc P., Ireland T.R., Harrison T.M., Foster J.J. and Bruce Z. (2009)**
Mass-spectrometric mining of Hadean zircons by automated SHRIMP multi-collector and single-collector U/Pb zircon age dating: The first 100,000 grains. *International Journal of Mass Spectrometry*, 286, 53–63.
- Horstwood M.S.A., Košler J., Gehrels G., Jackson S.E., McLean N.M., Paton C., Pearson N.J., Sircombe K., Sylvester P., Vermeesch P. and Bowring J.F. (2016)**
Community-derived standards for LA-ICP-MS U-(Th)-Pb geochronology – Uncertainty propagation, age interpretation and data reporting. *Geostandards and Geoanalytical Research*, 40, 311–332.
- Ibanez-Mejia M., Gehrels G.E., Ruiz J., Vervoort J.D., Eddy M.P. and Li C. (2014)**
Small-volume baddeleyite (ZrO₂) U-Pb geochronology and Lu–Hf isotope geochemistry by LA-ICP-MS. Techniques and applications. *Chemical Geology*, 384, 149–167.
- Johnston S., Gehrels G., Valencia V. and Ruiz J. (2009)**
Small-volume U-Pb zircon geochronology by laser ablation-multi-collector-ICP-MS. *Chemical Geology*, 259, 218–229.
- Kohn M.J., Engi M. and Lanari P. (editors) (2019)**
Petrochronology: Methods and applications (Volume 83). The Mineralogical Society of America (Chantilly, VA).
- Košler J. and Sylvester P.J. (2003)**
Present trends and the future of zircon in geochronology: Laser ablation ICP-MS. *Reviews in Mineralogy and Geochemistry*, 53, 243–275.
- Kylander-Clark A.R. (2017)**
Petrochronology by laser ablation-inductively coupled plasma-mass spectrometry. *Reviews in Mineralogy and Geochemistry*, 83, 183–198.
- Licht A., Pullen A., Kapp P., Abell J. and Giesler N. (2016)**
Eolian cannibalism: Reworked loess and fluvial sediment as the main sources of the Chinese Loess Plateau. *Geological Society of America Bulletin*, 128, 944–956.
- Mathews W.A. and Guest B. (2017)**
A practical approach for collecting large-*n* detrital zircon U-Pb data sets by quadrupole LA-ICP-MS. *Geostandards and Geoanalytical Research*, 41, 161–180.
- Mattinson J.M. (2005)**
Zircon U-Pb chemical abrasion (“CA-TIMS”) method: Combined annealing and multi-step partial dissolution analysis for improved precision and accuracy of zircon ages. *Chemical Geology*, 220, 47–66.
- Mattinson J.M. (2010)**
Analysis of the relative decay constants of ²³⁵U and ²³⁸U by multi-step CA-TIMS measurements of closed-system natural zircon samples. *Chemical Geology*, 275, 186–198.
- McKenzie N.R., Horton B.K., Loomis S.E., Stockli D.F., Planavsky N.J. and Lee C.T.A. (2016)**
Continental arc volcanism as the principal driver of icehouse-greenhouse variability. *Science*, 352, 444–447.
- Meinhold G., Morton A.C. and Avigad D. (2013)**
New insights into peri-Gondwana paleogeography and the Gondwana super-fan system from detrital zircon U-Pb ages. *Gondwana Research*, 23, 661–665.
- Moecher D.P. and Samson S.D. (2006)**
Differential zircon fertility of source terranes and natural bias in the detrital zircon record: Implications for sedimentary provenance analysis. *Earth and Planetary Science Letters*, 247, 252–266.
- Morton A.C., Clauoué-Long J.C. and Berge C. (1996)**
SHRIMP constraints on sediment provenance and transport history in the Mesozoic Stafford Formation, North Sea. *Journal of the Geological Society, London*, 153, 915–929.
- Murphy J.B., Fernández-Suárez J., Keppie J.D. and Jeffries T.E. (2004)**
Contiguous rather than discrete Paleozoic histories for the Avalon and Meguma terranes based on detrital zircon data. *Geology*, 32, 585–588.
- Paces J.B. and Miller J.D. Jr. (1993)**
Precise U-Pb ages of Duluth complex and related mafic intrusions, northeastern Minnesota: Geochronological insights to physical, petrogenetic, paleomagnetic, and tectonomagmatic processes associated with the 1.1 Ga midcontinent rift system. *Journal of Geophysical Research: Solid Earth*, 98, 13997–14013.
- Paton C., Hellstrom J., Paul B., Woodhead J. and Hergt J. (2011)**
Lolite: Freeware for the visualisation and processing of mass spectrometric data. *Journal of Analytical Atomic Spectrometry*, 26, 2508–2518.



references

Pettit B.S., Blum M., Pecha M., McLean N., Bartschi N.C. and Saylor J.E. (2019)

Detrital-zircon U-Pb paleodrainage reconstruction and geochronology of the Campanian Blackhawk-Castlegate succession, Wasatch Plateau and Book Cliffs, Utah, USA. *Journal of Sedimentary Research*, **89**, 273–292.

Pullen A., Ibáñez-Mejía M., Gehrels G.E., Giesler D. and Pecha M. (2018)

Optimization of a laser ablation-single collector-inductively coupled plasma-mass spectrometer (Thermo Element 2) for accurate, precise, and efficient zircon U-Th-Pb geochronology. *Geochemistry Geophysics Geosystems*, **19**, 3689–3705.

Pullen A., Ibáñez-Mejía M., Gehrels G.E., Ibáñez-Mejía J.C. and Pecha M. (2014)

What happens when $n = 1000$? Creating large- n geochronological datasets with LA-ICP-MS for geologic investigations. *Journal of Analytical Atomic Spectrometry*, **29**, 971–980.

Reiners P.W. (2005)

Zircon (U-Th)/He thermochronometry. *Reviews in Mineralogy and Geochemistry*, **58**, 151–179.

Satkoski A.M., Wilkinson B.H., Hietpas J. and Samson S.D. (2013)

Likeness among detrital zircon populations – An approach to the comparison of age frequency data in time and space. *Geological Society of America Bulletin*, **125**, 1783–1799.

Saylor J.E., Stockli D.F., Horton B.K., Nie J. and Mora A. (2012)

Discriminating rapid exhumation from syndepositional volcanism using detrital zircon double dating: Implications for the tectonic history of the Eastern Cordillera, Colombia. *Geological Society of America Bulletin*, **124**, 762–779.

Saylor J.E. and Sundell K.E. (2016)

Quantifying comparison of large detrital geochronology data sets. *Geosphere*, **12**, 203–220.

Saylor J.E., Sundell K.E. and Sharman G.R. (2019)

Characterizing sediment sources by non-negative matrix factorization of detrital geochronological data. *Earth and Planetary Science Letters*, **512**, 46–58.

Schmitz M.D. and Bowring S.A. (2001)

U-Pb zircon and titanite systematics of the Fish Canyon Tuff: An assessment of high-precision U-Pb geochronology and its application to young volcanic rocks. *Geochimica et Cosmochimica Acta*, **65**, 2571–2587.

Schoene B. (2014)

U-Th-Pb geochronology. *Treatise on Geochemistry*, **4**, 341–378.

Schoene B., Crowley J.L., Condon D.J., Schmitz M.D. and Bowring S.A. (2006)

Reassessing the uranium decay constants for

geochronology using ID-TIMS U-Pb data. *Geochimica et Cosmochimica Acta*, **70**, 426–445.

Shaulis B., Lapen T.J. and Toms A. (2010)

Signal linearity of an extended range pulse counting detector: Applications to accurate and precise U-Pb dating of zircon by laser ablation quadrupole ICP-MS. *Geochemistry Geophysics Geosystems*, **11**, 1–12.

Sircombe K.N. (1999)

Tracing provenance through the isotope ages of littoral and sedimentary detrital zircon, eastern Australia. *Sedimentary Geology*, **124**, 47–67.

Sláma J., Košler J., Condon D.J., Crowley J.L., Gerdes A., Hancher J.M., Horstwood M.S.A., Morris G.A., Nasdala L., Norberg N. and Schaltegger U. (2008)

Plešovice zircon – A new natural reference material for U-Pb and Hf isotopic microanalysis. *Chemical Geology*, **249**, 1–35.

Soreghan M.J. and Gehrels G.E. (editors) (2000)

Paleozoic and Triassic paleogeography and tectonics of western Nevada and northern California. *Geological Society of America (Volume 347)*. Geological Society of America (Boulder, CO).

Soreghan M.J., Soreghan G.L. and Hamilton M.A. (2002)

Paleowinds inferred from detrital-zircon geochronology of upper Paleozoic loessite, western equatorial Pangea. *Geology*, **30**, 695–698.

Speer J.A. (1980)

Zircon. *Reviews in Mineralogy and Geochemistry*, **5**, 67–112.

Stacey J.T. and Kramers J. (1975)

Approximation of terrestrial lead isotope evolution by a two-stage model. *Earth and Planetary Science Letters*, **26**, 207–221.

Stem R.A., Bodorkos S., Kamo S.L., Hickman A.H. and Corfu F. (2009)

Measurement of SIMS instrumental mass fractionation of Pb isotopes during zircon dating. *Geostandards and Geoanalytical Research*, **33**, 145–168.

Stockli D.F. (2005)

Application of low-temperature thermochronometry to extensional tectonic settings. *Reviews in Mineralogy and Geochemistry*, **58**, 411–448.

Sundell K.E. and Saylor J.E. (2017)

Unmixing detrital geochronology age distributions. *Geochemistry Geophysics Geosystems*, **18**, 2872–2886.

Thomson S.N., Gehrels G.E., Ruiz J. and Buchwaldt R. (2012)

Routine low-damage apatite U-Pb dating using laser ablation-multicollector-ICPMS. *Geochemistry, Geophysics, Geosystems*, **13**(2), 1–23.

references

Vermeesch P. (2004)

How many grains are needed for a provenance study? *Earth and Planetary Science Letters*, 224, 441–451.

Vermeesch P. (2013)

Multi-sample comparison of detrital age distributions. *Chemical Geology*, 341, 140–146.

Viete D.R., Kylander-Clark A.R. and Hacker B.R. (2015)

Single-shot laser ablation split stream (SS-LASS) petrochronology deciphers multiple, short-duration metamorphic events. *Chemical Geology*, 415, 70–86.

Wendt I. and Carl C. (1991)

The statistical distribution of the mean squared weighted deviation. *Chemical Geology (Isotope Geoscience section)*, 86, 275–285.

Whitchurch A.L., Carter A., Sinclair H.D., Duller R.A., Whittaker A.C. and Allen P.A. (2011)

Sediment routing system evolution within a diachronously uplifting orogen: Insights from detrital zircon thermochronological analyses from the south-central Pyrenees. *American Journal of Science*, 311, 442–482.

Wiedenbeck M., Allé P., Corfu F., Griffin W.L., Meier M., Oberli F., von Quadt A., Roddick J.C. and Spiegel W. (1995)

Three natural zircon standards for U-Th-Pb, Lu-Hf, trace element and REE analyses. *Geostandards Newsletter*, 19, 1–23.

Wiedenbeck M., Hanchar J.M., Peck W.H., Sylvester P., Valley J., Whitehouse M., Kronz A., Morishita Y., Nasdala L., Fiebig J. and Franchi I. (2004)

Further characterisation of the 91500 zircon crystal. *Geostandards and Geoanalytical Research*, 28, 9–39.

Willigers B.J.A., Baker J.A., Krogstad E.J. and Peate D.W. (2002)

Precise and accurate *in situ* Pb-Pb dating of apatite, monazite and sphene by laser ablation multiple-collector ICP-MS. *Geochimica et Cosmochimica Acta*, 66, 1051–1066.

Zadnik M.G., Specht S. and Begemann F. (1989)

Revised isotopic composition of terrestrial mercury. *International Journal of Mass Spectrometry and Ion Processes*, 89, 103–110.

Supporting information

The following supporting information may be found in the online version of this article:

Appendix S1 U-Pb measurement results.

Appendix S2 Indexing information.

This material is available from: <http://onlinelibrary.wiley.com/doi/10.1111/ggr.12355/abstract> (This link will take you to the article abstract).

